ACS APPLIED NANO MATERIALS
Cite This: ACS Appl. Nano Mater. 2019, 2, 4942−4953
Article
www.acsanm.org

Plasmonic Aluminum Nanohole Arrays as Transparent Conducting Electrodes for Organic Ultraviolet Photodetectors with Bias-Dependent Photoresponse

Monica R. Esopi and Qiuming Yu*

Department of Chemical Engineering, University of Washington, Seattle, Washington 98195, United States

Supporting Information

ABSTRACT: Electrodes consisting of plasmonic Al nanohole arrays (Al-NHAs) were incorporated into organic ultraviolet (UV) photodetectors that exhibited bias-dependent photoresponse. Al-NHAs were designed by using three-dimensional finite-difference time-domain (3D-FDTD) simulations to produce strong UV absorbance in the active layer and enhanced internal electric field intensity. The nanosphere lithography fabricated Al-NHAs were incorporated into organic conventional devices, which produced two narrow response peaks under reverse bias and one broad response peak under forward bias, while ITO-based control devices can only produce two-peak photoresponse spectra. The bias-dependent photoresponse switching achieved by the Al-NHA-based devices is attributed to the plasmonic-enhanced internal electric field, which acts as a small forward bias and increases the driving force for hole diffusion. Conventional devices with planar Al electrodes and hole-only devices with both planar Al and an Al-NHA electrodes were also fabricated and evaluated to confirm the photoresponse mechanism. Plasmonic Al-NHA electrodes provide an approach for making ITO-free, flexible organic UV photodetectors with improved photoresponse and bias-dependent response tunability.

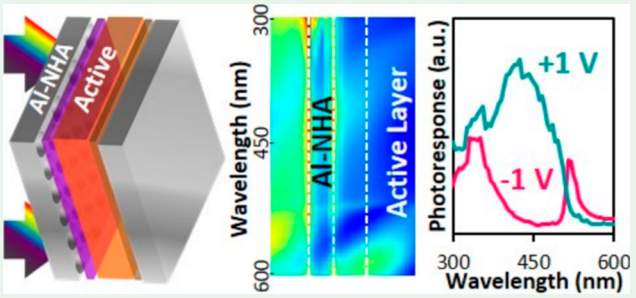

KEYWORDS: *plasmonic nanostructures, organic photodetectors, tunable photoresponse, ITO-free, ultraviolet photodetectors*

INTRODUCTION

Metallic nanostructured films incorporated into optoelectronic devices such as photodetectors have attracted attention for their ability to support localized surface plasmon polaritons (LSPPs), which can enhance optical absorbance, internal electric field, and ultimately device performance.[1−3] Such films can also act as a device electrode, making them a cost-effective, flexible, high-performance alternative to the commonly used indium tin oxide (ITO), which is expensive and brittle.[4,5] Plasmonic enhancements provided by nanostructured electrodes can be engaged by light of varying wavelengths depending on the geometry, periodicity, and material of the nanostructures.[3,6−10] This provides a mechanism for tuning and enhancing the spectral photoresponse of optoelectronic devices, making plasmonic nanostructures attractive for a wide variety of applications including solar cells, fiber-optic communications, displays, disk drives, motion sensors, filter-free imaging, flame and missile detection, environmental monitoring, and industrial process control.[11−16]

Plasmonic nanostructures have been employed effectively in thin film solar cells, enabling devices with thinner active layers, which have superior charge transport properties, to compete optically with thicker devices by improving absorption through light scattering, local electric field enhancement, and light trapping.[6] This heightened absorption increases the short circuit density (J_{SC}) produced by thin film solar cells that incorporate plasmonic nanostructures, therefore improving device performance. Thin film perovskite solar cells, having a structure of fluorine-doped tin oxide (FTO)/TiO_2/$CH_3NH_3PbI_3$/2,2′,7,7′-tetrakis(*N*,*N*-di-4-methoxyphenylamino)-9,9′-spirobifluorene (spiro-OMeTAD)/Au, produced a J_{SC} of 13.19 mA cm^{-2} when plasmonic Ag nanoparticles were deposited between the FTO and TiO_2 layers compared to 10.79 mA cm^{-2} when no Ag nanoparticles were included.[17] Additionally, an Au nanohole array (Au-NHA) was shown to improve the J_{SC} with respect to active layer thickness when incorporated into inverted organic solar cells with a device structure of Au-NHA/ZnO/poly[[4,8-bis[(2-ethylhexyl)oxy]benzo[1,2-*b*:4,5-*b*′]dithiophene-2,6-diyl][3-fluoro-2-[(2-ethylhexyl)carbonyl]thieno[3,4-*b*]thiophenediyl]] (PTB7):phenyl-C_{71}-butyric acid methyl ester ($PC_{71}BM$)/MoO_3/Ag.[4] The nanostructured electrode improved absorption in the active layer by trapping light via an optical cavity effect and thus enabled J_{SC} levels to be maintained when the active layer was decreased to suboptimal thickness, offering a potential solution to the trade-off between

Received: May 13, 2019
Accepted: August 1, 2019
Published: August 1, 2019

DOI: 10.1021/acsanm.9b00902
ACS Appl. Nano Mater. 2019, 2, 4942−4953

optical absorption and charge extraction that persists in thin film solar cells.[4] Plasmonic nanostructures were also incorporated into the rear electrode of a similar organic solar cell with a structure of ITO/ZnO/PTB7:$PC_{71}BM$/MoO_3/Ag by imprinting into the top surface of the soft polymer active layer, resulting in J_{SC} values of 15.17 and 14.01 mA cm^{-2} for patterned and nonpatterned devices, respectively.[18]

The coupling of light and surface charge into LSPPs enhances the electric field at both interfaces of the plasmonic electrode.[19] This phenomenon is very attractive for photodetectors, particularly those relying on charge injection and transport at device electrode interfaces.[3,7] Photodetectors utilizing plasmonic nanostructures produce improved responsivity (R), which measures the output current compared to the incident optical power, and improved spectral photoresponse selectivity.[3] Imprinting a nanograting pattern directly into the perovskite ($CH_3NH_3PbI_3$) active layer of a lateral metal−semiconductor−metal photodetector resulted in a 30-fold increase in R, compared to nonimprinted devices, yielding a peak value of 58.5 A W^{-1} under 635 nm illumination and a 1 V bias.[20] Another lateral perovskite ($CH_3NH_3PbI_3$) photodetector incorporated plasmonic nanostructures into its multilayered substrate of Au nanosquares/SiO_2/Au, compared to a control substrate of Si/SiO_2, which would act similarly to a rear nanostructured electrode in a vertical device architecture.[21] The nanosquare arrays coupled with incident light to improve light absorption, resulting in about a 50-fold photocurrent enhancement under a 0.5 V bias and incident illumination with wavelengths around both 725 and 800 nm.[21] Nanoparticles have also been incorporated into organic photodetectors and have yielded significant performance improvements. A device with a structure of ITO/4,4-*N*,*N*′-bis[*N*-(1-naphthyl)-*N*-phenylamino]biphenyl (NPB)/C_{60}/bathocuproine (BCP)/Al incorporated Au nanoparticles at the top of the NPB active layer, and through plasmonic enhancements to the absorption and local electric field as well as hot carrier injection, the R values increased from 2.00 to 99.38 mA W^{-1} under 830 nm illumination and a −0.4 V bias.[22] In these devices, plasmonic excitements enable some sub-bandgap photodetection, and this can also be pursued as the main design objective. An Ag nanohole array (Ag-NHA) was incorporated into the bottom transparent electrode of a device with a structure of Ag-NHA/2,2′,7,7′-tetrakis(*N*,*N*′-di-*p*-methylphenylamino)-9,9′-spirobifluorene (spiro-TTB)/Al and improved the photoresponse strength by 2 orders of magnitude under 830 nm illumination and a 5 V bias.[23]

Photodetectors that are sensitive to UV illumination are important in a variety of applications including environmental monitoring, scientific research, imaging, and flame and missile detection.[14−16] Despite their applicability, the extension of plasmonic enhancement mechanisms to UV-selective devices has been relatively slow because the common plasmonic metals of Ag and Au cannot support surface plasmon polaritons (SPPs) when illuminated by light with wavelengths shorter than about 350 nm.[24] Al is well-suited to support and tune SPPs in the UV spectral range due to its carrier concentration and dielectric function, although oxide formation on the Al surface can interfere with and cause a red shift in its plasmonic properties.[24−30] In addition, Al provides an attractive material option for UV photodetectors due to its relative abundance and low cost compared to Ag and Au. A simulated Al nanogrid demonstrated optical transmittance that could be tuned between about 300 and 430 nm by varying the geometry of the grid,[29] and Al nanoparticle arrays produced plasmonic resonance peaks that could be shifted between about 270−340 nm by varying the particle size.[30] Acting as a hot electron injection material, plasmonic Al can provide performance enhancements both within and beyond the UV spectral range. A device consisting of Al and ITO electrodes separated by a thin Al_2O_3 layer produced a peak R value of 250 nA W^{-1} under 440 nm illumination and no bias.[25] Incorporating plasmonic Al nanowires into the same device resulted in significant enhancements to the sub-bandgap absorption, demonstrating that plasmonic Al nanostructures could improve solar cell performance in addition to photodetection.[25] In fact, simulated organic solar cells with a device structure of Al nanohole array (Al-NHA)/poly(3,4-ethylenedioxythiophene):polystyrenesulfonate (PEDOT:PSS)/poly(3-hexylthiophene) (P3HT):$PC_{61}BM$/ZnO/perfect electronic conductor (PEC) were reported to have enhanced absorbance throughout the visible range, compared to devices based on ITO, that could be precisely tuned by varying both the geometry of the Al-NHA and the thickness of the device layers, utilizing the optical cavity effect of the multilayered device.[31] Because of its plasmonic properties and ability to induce sub-bandgap photoresponse, Al can be used as a filter for color-selective photoresponse throughout the UV and visible spectral ranges. An Al grating deployed on top of a lateral photodetector, utilizing Al electrodes on a Si substrate with a thin oxide layer, was reported as an effective color-selective filter, as grating pitch values of 300, 400, and 500 nm resulted in blue, green, and red photodetection, respectively.[32]

In this work, Al nanohole arrays (Al-NHAs) were utilized as transparent conducting electrodes to optimize the UV-selectivity and response tunability of photodetectors having a conventional photodiode structure with organic active materials, which provide a low-cost, flexible alternative to inorganic materials.[16] UV-selectivity was ensured through the material selection of Al, for plasmonic activity within the UV spectral range, and the polymer donor of poly(9,9-dioctylfluorene-*alt*-bithiophene) (F8T2), for strong UV absorption with a cutoff around 515 nm. The active layer was a 350 nm film consisting of F8T2 and the fullerene-derivative electron acceptor $PC_{71}BM$, combined in a weight ratio of 100:4, based on previous reports.[33] PEDOT:PSS and LiF were used as hole and electron transport layers, respectively, for an overall device structure of Al-NHA/PEDOT:PSS/F8T2:$PC_{71}BM$/LiF/Al. 3-dimensional finite-difference time-domain (3D-FDTD) electromagnetic simulations were conducted to design the Al-NHA to produce strong UV absorption in the active layer and enhanced internal electric field intensity. Al-NHA electrodes were successfully fabricated using nanosphere lithography and incorporated into photodetectors, which produced two narrow photoresponse peaks with specific detectivity (D^*) values of 4.0×10^9 and 4.6×10^9 jones under 340 and 515 nm illumination, respectively, and −2 V bias and one broad photoresponse peak with a peak D^* of 8.8×10^9 jones under 450 nm illumination and 2 V bias. Compared to control ITO-based devices, Al-NHA-based devices had similar response under reverse bias and superior response under forward bias, as ITO-based devices became unstable under forward bias. The bias-dependent photoresponse switching is believed to benefit from the plasmonic-enhanced internal electric field, which increases the driving force for hole diffusion. The mechanism was further confirmed by the investigation of conventional devices with planar Al electrodes and hole-only devices with

DOI: 10.1021/acsanm.9b00902
ACS Appl. Nano Mater. 2019, 2, 4942−4953

both planar Al and Al-NHA electrodes. This novel bias-dependent response switching improves the applicability of UV photodetectors through the cost-effective, flexible, and performance-enhancing plasmonic Al-NHA transparent conducting electrodes.

EXPERIMENTAL SECTION

3D-FDTD Simulations. Three-dimensional, finite-difference time-domain (3D-FDTD) electromagnetic simulations (Lumerical, Inc.) were used to study conventional devices based on Al-NHA, Al^{Planar}, and ITO electrodes. The simulated device structure was Corning EAGLE XG glass (100 nm)/[Al-NHA (30 nm) or ITO (200 nm)]/PEDOT:PSS (40 nm)/F8T2:$PC_{71}BM$ (350 nm)/LiF (0.8 nm)/Al (100 nm). The NHA had a diameter (D) and pitch (p) defined as the nanohole diameter and the center-to-center distance, respectively. A hexagonal array was simulated, so the x and y spans of the simulation cell were defined as p and $p\sqrt{3}$, respectively. A continuous wavelength plane wave light source (300−600 nm) was placed 600 nm below the device. The boundary conditions used in the x, y, and z directions were antisymmetric, symmetric, and perfectly matched layer, respectively, simulating a periodic array with free space above and below. The simulation was run with 250 frequency points, and the auto-shut-off limit was reached in all cases. An auto-non-uniform mesh was used, with the mesh accuracy set to 4 and a minimum mesh step of 0.25 nm used. Frequency-domain field monitors, which can capture both transmittance of light and electric field distribution, were placed throughout the device. Monitors between device layers were used to capture transmittance, and absorbance in a given layer was calculated by subtracting the transmittance above and below the specified layer. Monitors were also placed in vertical cross sections in the xz- and yz-planes, intersecting at (0,0), to capture the internal electric field distribution. A specific x−y point was chosen from each monitor so that the electric field could be plotted against incident wavelength. The wavelength-dependent optical constants of refractive index, n, and extinction coefficient, k, for ITO, PEDOT:PSS, F8T2:$PC_{71}BM$, and the glass substrate were experimentally measured via ellipsometry (Figure S1) and for Al and LiF were obtained from the Lumerical Materials Database[34] and an online database,[35,36] respectively.

Al-NHA Fabrication via Nanosphere Lithography. Carboxylate surface-functionalized polystyrene beads with a diameter of 200 nm were purchased from Polysciences, Inc. (Warrington, PA). The stock solution (5.68×10^{12} particles mL^{-1}) was diluted (1.43×10^{12} particles mL^{-1}) before use with ultrapure water (18 MΩ). Poly(ethylene oxide) (molecular weight 1000000 g mol^{-1}, Sigma-Aldrich, St. Louis, MO) was added at a concentration of 100 ppm. Corning EAGLE XG glass substrates, 1.1 mm thick, were cut into 1.5 cm × 1.5 cm squares and cleaned by ultrasonication for 15 min each in soapy deionized (DI) water, DI water, acetone, and isopropanol, sequentially, followed by 20 min of UV-ozone (UVO) treatment. Immediately after UVO treatment, 5 μL of the nanosphere suspension was dropped onto the substrates, which were then moved in gentle circular motions, to spread the suspension over the surface, before being laid flat to dry. Monolayer nanosphere films were etched with O_2 and Ar flow rates of 80 and 20 sccm (standard cubic centimeters per minute), respectively, at 125 W for 90 s using a plasma treatment system (Yield Engineering Systems, Inc. CV200RF Series). 30 nm of Al was deposited on etched spheres with a CHA Solution e-beam evaporator without any masks, and the film thickness was controlled by a quartz crystal microbalance (QCM). Nanosphere liftoff was performed via ultrasonication in toluene (99.8%, Sigma-Aldrich). Transmission of Al-NHA was measured with a xenon arc lamp and an Oriel Cornerstone 130 monochromator, a Newport 1918-R power meter, and a Newport UV-Si photodiode. A scanning electron microscope (SEM, FEI Sirion) was used to characterize the nanostructures in each step.

Device Fabrication and Characterization. ITO-coated Corning EAGLE XG glass substrates (≤10 Ω sq^{-1}, Colorado Concept Coatings LLC, Loveland, CO) were cut into 1.5 cm × 1.5 cm squares and cleaned by the same procedure described above. Al-NHA electrodes were prepared as previously described. Al^{Planar} electrodes were fabricated by depositing 10 nm of Al (99.999%, R.D. Mathis, Long Beach, CA) onto cleaned Corning EAGLE XG glass substrates via thermal evaporation. All three types of electrodes were exposed to UVO treatment to improve the hydrophilicity. PEDOT:PSS solution (Clevios P VP AI 4083, Heraeus, Hanau, Germany) was filtered through a 0.45 μm PTFE syringe filter and deposited via spin-coating at 5000 rpm for 40 s, followed by baking at 120 °C for 10 min in air. The chips were then transferred into a nitrogen-filled glovebox, where active layers were deposited from a previously prepared precursor solution. F8T2 (molecular weight of 29000 g/mol, polydispersity index of 3.3, American Dye Source, Baie D'Urfe, Quebec, Canada) and $PC_{71}BM$ (Nano-C Inc., Westwood, MA) were dissolved separately in 1,2-dichlorobenzene (anhydrous, 99.9%, Sigma-Aldrich) at a concentration of 40 mg mL^{-1} and stirred at 700 rpm and 70 °C for at least 12 h and then combined into a F8T2:$PC_{71}BM$ (weight ratio 100:4) precursor solution, which was stirred for at least an additional 1 h at 700 rpm and 70 °C before being filtered through a 0.2 μm PTFE syringe filter. The active layer was formed via spin-coating the precursor solution at 1000 rpm for 30 s and then annealed at 80 °C for 10 min. A thin 0.8 nm layer of LiF (99.995%, Sigma-Aldrich) or 10 nm MoO_3 (99.9995%, Alfa Aesar, Haverhill, MA) for hole-only devices followed by 100 nm Al was deposited via thermal evaporation using an Angstrom Engineering Amod PVD platform. LiF and MoO_3 were deposited without the use of any mask; Al electrodes were deposited with circular masks so that the active area of each device was 0.03 cm^2, and 16 devices were on each chip. The thicknesses of LiF, MoO_3, and Al were controlled by QCM during evaporation. All device characterization measurements were performed in air. J−V curves, dark current over time, EQE spectra, and response speed were obtained by using a Keithley 2635B sourcemeter. Light for these measurements as well as transmission and reflection measurements was provided using a xenon arc lamp and an Oriel Cornerstone 130 monochromator. Optical intensity was measured by using a Newport 1918-R power meter and a Newport UV-Si photodiode. The response speed was obtained by manually switching between dark/light conditions. The active layer film thickness was measured by using a KLA Tencor Alpha-Step 500 profiler, and ITO and PEDOT:PSS film thicknesses were confirmed during ellipsometry measurements. Sheet resistance was measured by using a Jandel cylindrical four-point probe connected with a Keithley 2450 sourcemeter. UV−vis spectroscopy data were collected by using a PerkinElmer Lambda 900 UV−vis spectrophotometer.

RESULTS AND DISCUSSION

Design and Evaluation of Al-NHAs via 3D-FDTD Simulations. An overview of the 3D-FDTD simulation setup used to design the Al-NHA electrodes is shown in Figure 1. The bottom-illuminated conventional device with a structure of Al-NHA (30 nm)/PEDOT:PSS (40 nm)/

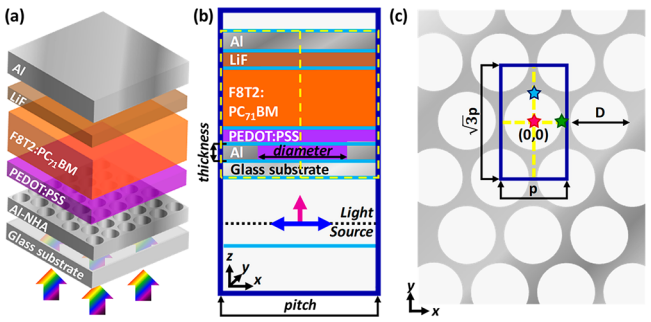

Figure 1. (a) Illustration of a conventional Al-NHA-based device. (b) A cross-sectional view of a simulation unit cell. (c) A top view of the hexagonal Al-NHA.

DOI: 10.1021/acsanm.9b00902
ACS Appl. Nano Mater. 2019, 2, 4942−4953

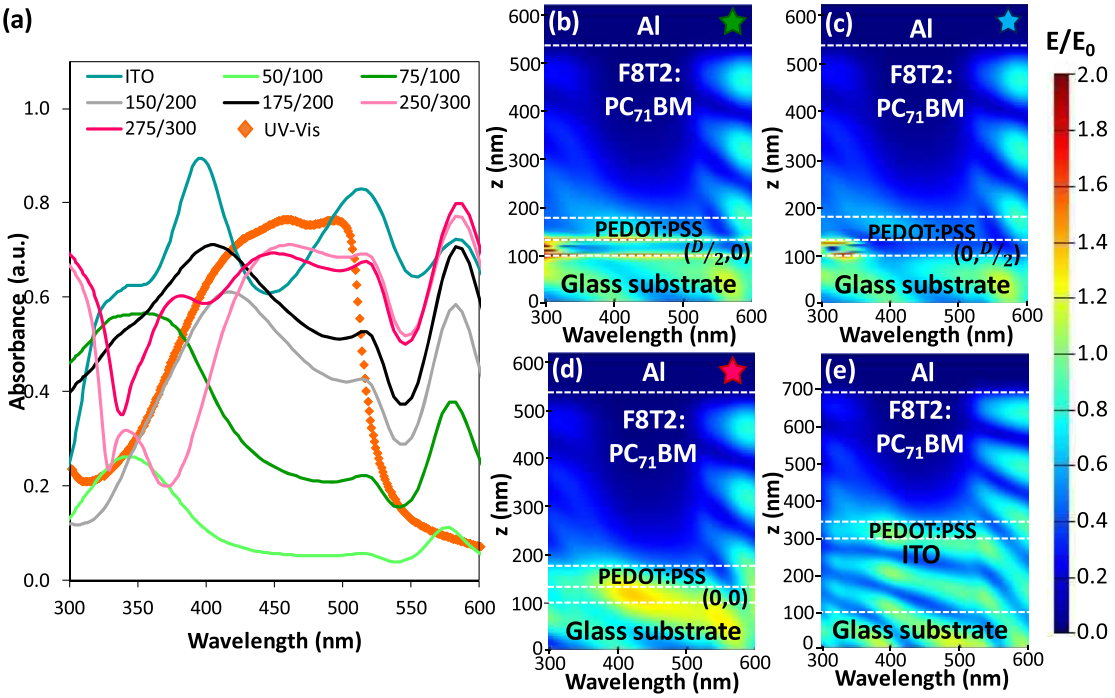

Figure 2. (a) 3D-FDTD-simulated active layer absorbance spectra for Al-NHA-based devices and an ITO-based device with experimental UV−vis absorption spectrum of F8T2:$PC_{71}BM$ thin film superimposed. (b−d) 3D-FDTD-simulated internal electric field distributions as a function of wavelength for an Al-NHA-based device with a diameter/pitch of 175/200 nm at the x−y coordinate of (b) (D/2, 0), (c) (0, D/2), and (d) (0, 0) based on the coordinates defined in Figure 1c and marked as green, blue, and pink stars, respectively. (e) 3D-FDTD-simulated internal electric field distribution as a function of wavelength for an ITO-based device at any x−y point. The reference electric field (E_0) is 1 V/m.

F8T2:$PC_{71}BM$ (350 nm, 100:4 weight ratio)/LiF (0.8 nm)/Al (100 nm) is illustrated in Figure 1a. A cross-sectional view of the simulation unit cell is shown in Figure 1b, where the simulation boundary is represented by a blue border and the light source impinges normally from the bottom of the device with polarization in the x-direction. Optical power monitors, indicated by light blue lines, were placed between the device layers to obtain the transmittance. The absorbance within each layer was calculated by subtracting the transmittance at the bottom from that at the top. Additional optical power monitors, indicated by dashed yellow lines, were placed in vertical cross sections in the x−z and y−z planes, intersecting at the x−y origin (0, 0) to obtain the internal electric field distribution throughout the device. A top view of the hexagonal Al-NHA is shown in Figure 1c, indicating the x−y origin (0, 0), nanohole diameter (D), and unit cell length in the x- and y-directions, pitch (p) and $p\sqrt{3}$, respectively.

Devices based on Al-NHA electrodes with diameter/pitch combinations of 50/100 nm, 75/100 nm, 150/200 nm, 175/200 nm, 250/300 nm, and 275/300 nm were simulated, and the results are presented in Figure 2. The simulated active layer absorbance for these Al-NHA-based devices, as well as for an ITO-based device, is shown in Figure 2a. UV−vis measurements were performed on an F8T2:$PC_{71}BM$ film (350 nm thick, 100:4 weight ratio), and an absorption spectrum is superimposed in Figure 2a for comparison and to indicate the photoactive range of the active layer. For all devices, the simulated active layer absorbance shows a clear cutoff around 530 nm, which aligns relatively well with the cutoff of the UV−vis absorption spectrum. A peak around 580 nm, outside of the active layer absorption range, is observed for all simulated devices due to the nanocavity effect resulting from the top reflective Al electrode. To confirm this, the absorbance of the active layer for both Al-NHA- and ITO-based devices without the top Al layer was simulated, and the results (Figure S2) do not show this peak at 580 nm. UV-selective plasmon-enhanced absorbance peaks around 350−400 nm are shown for Al-NHA-based devices with smaller pitches (100−200 nm). For the ITO-based device, peaks around 400, 515, and 580 nm and dips around 445 and 555 nm were observed, which correspond respectively to dips and peaks in the total reflectance at the same wavelengths (Figure S3). This behavior is attributed to reflectance resulting from the multilayered device structure and subsequent cavity effects.

The Al-NHA electrode with a diameter/pitch of 50/100 nm produces the lowest active layer absorbance because the volume fraction of nanoholes in the Al-NHA film is only 23%, resulting in low transmittance. Increasing the diameter to 75 nm, while keeping the same pitch of 100 nm, increases the volume fraction of nanoholes in the Al-NHA film to 51%. While hole volume fraction alone does not determine the final magnitude and spectral shape of electrode transmittance, which is also affected directly by the geometry of the nanopattern, increasing the hole volume fraction does correspond to an increase in transmittance, which in turn results in higher absorbance in the active layer. Therefore, the electrode with a diameter/pitch of 75/100 produces active layer absorbance that is spectrally similar to that produced by the 50/100 electrode but is higher in magnitude. Because surface plasmon resonance is sensitive to the nanoarray pitch,[3,38] a red shift of transmittance through Al nanogrids[29] and active layer absorbance of solar cells based on Au-NHA electrodes[4] were reported when the nanopattern pitch was increased. The same trend is observed for the devices represented in Figure 2a. When the pitch is increased from 100 to 200 nm, the plasmon-enhanced absorption peak shifts

DOI: 10.1021/acsanm.9b00902
ACS Appl. Nano Mater. 2019, 2, 4942−4953

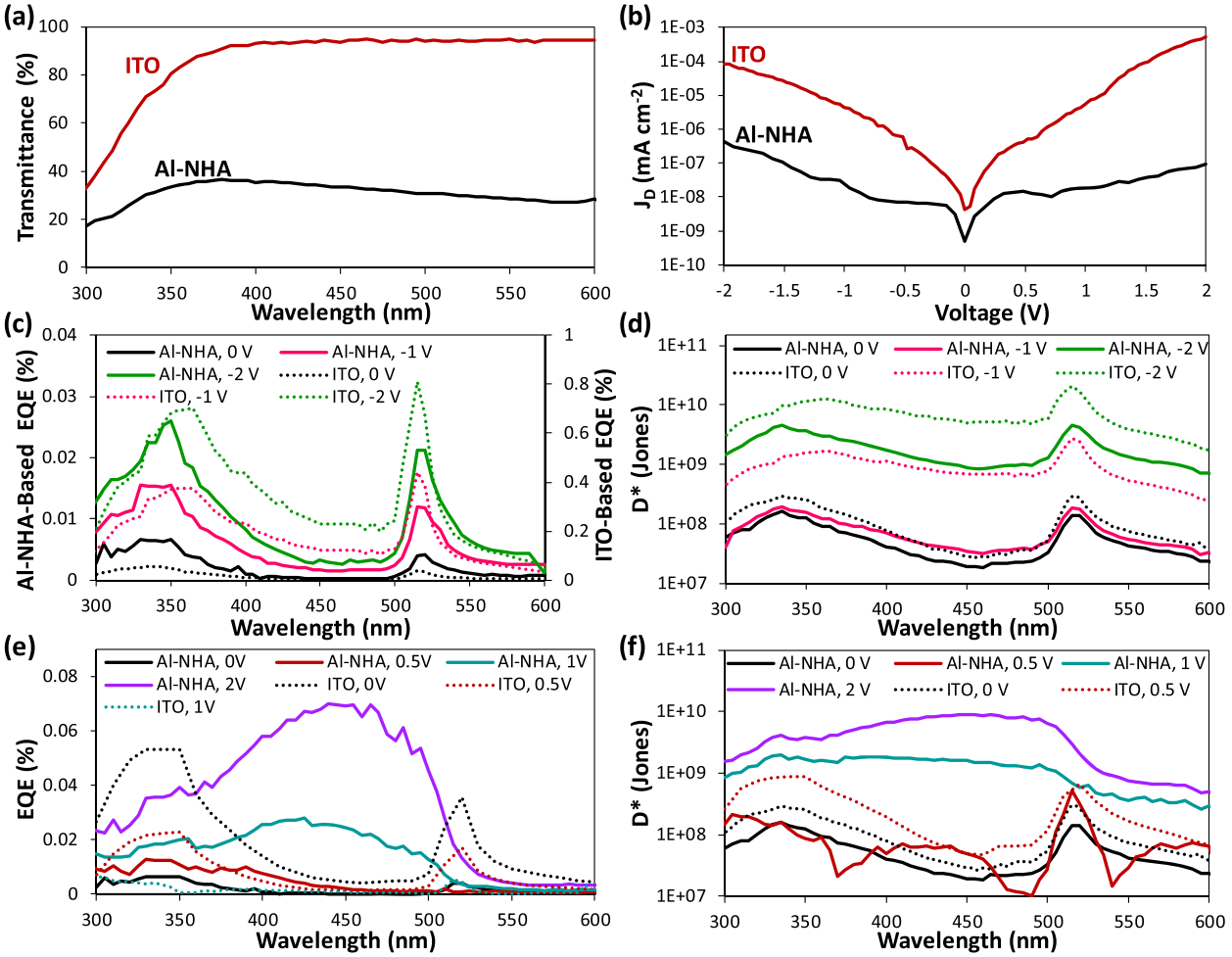

Figure 3. (a) Transmittance spectra for Al-NHA and ITO electrodes. (b) Dark current density−voltage curves for Al-NHA- and ITO-based devices. (c, d) EQE and *D** spectra for Al-NHA- and ITO-based devices under reverse biases. (e, f) EQE and *D** spectra for Al-NHA- and ITO-based devices under forward biases.

from around 350 nm to around 400 nm, maintaining UV selectivity despite this red shift. For Al-NHA films with a diameter/pitch of 150/200 nm and 175/200 nm, the volume fractions of nanoholes are 51% and 69%, respectively. For this pitch, increasing the diameter also increases the magnitude of the active layer absorbance produced, particularly in the UV spectral range between about 300 and 400 nm. Increasing the pitch further to 300 nm results in a further red shift of plasmon-enhanced absorbance, and the plasmonic peaks merge with the active layer absorbance between about 450 and 515 nm. The volume fractions of nanoholes in Al-NHA films with a diameter/pitch of 250/300 and 275/300 are 63% and 76%, respectively, and the absorbance of the active layer between 450 and 515 nm hardly changes when the diameter is increased.

With a few exceptions, the ITO-based control device produces stronger active layer absorbance than most of the Al-NHA-based devices due to the relatively high transmittance of ITO compared to Al-NHAs. Electrodes with a pitch of 300 nm produce higher active layer absorbance values than ITO in the spectral range between about 425 and 475 nm, and the electrode with a diameter/pitch of 175/200 nm yields active layer absorbance values at its peak, around 400 nm, that are competitive with ITO. In fact, this 175/200 nm electrode yields stronger active layer absorbance values than any other Al-NHA in the spectral range between about 360 and 425 nm. Therefore, the Al-NHA-based device with a diameter/pitch of 175/200 nm shows clear UV-selective plasmon-enhanced absorbance and strong active layer absorbance overall, so we chose this as the optimal geometry for pursuit in further theoretical investigation and device incorporation.

To provide more insight into device photoresponse mechanisms related to where within the active layer light of different wavelengths is absorbed and where the electric field is most intense, the wavelength-dependent electric field distributions of Al-NHA- and ITO-based devices were also simulated by using 3D-FDTD simulations (Figure 2b−e). An Al-NHA film with a diameter/pitch of 175/200 nm was used for the Al-NHA-based device. The electric field is mapped along the *z* direction of each device, for a specific *x*−*y* point, against the incident illumination wavelength. For the Al-NHA-based device, electric field distributions at three *x*−*y* points, corresponding to the *x*-edge, *y*-edge, and center point of the central nanohole, were calculated to provide a representative evaluation of the internal electric field throughout the device. The wavelength-dependent electric field distributions at *x*−*y* points of (*D*/2, 0), (0, *D*/2), and (0,0) based on the coordinates defined in Figure 1c and marked by green, blue, and pink stars in Figures 2b, 2c, and 2d, respectively.

DOI: 10.1021/acsanm.9b00902
ACS Appl. Nano Mater. 2019, 2, 4942−4953

Because plasmonic enhancement to the internal electric field is a near-field effect,[7] any influence of the Al-NHA electrode on the electric field distribution would occur in the lower portion of the device, near the PEDOT:PSS interface. Distinct behavior is observed from the Al-NHA-based device at each of the three $x-y$ points in Figure 2b−d due to the hexagonal NHA, the coupling of SPPs, and the polarization of incident light. In general, relatively strong electric fields occur at the interfaces of PEDOT:PSS/Al-NHA and Al-NHA/glass, as demonstrated by the red areas along the Al-NHA interfaces observed at the x- and y-edges of the nanohole, shown in Figures 2b and 2c, respectively. Notably, the highest electric field intensities are obtained when incident illumination has wavelengths between about 300 and 500 nm, which aligns well with the UV−vis absorbance spectrum and intended spectral range of photodetection. The ITO-based device, shown in Figure 2e, produces notable oscillations in the electric field intensity within the ITO and glass layers in the wavelength range corresponding to active layer absorption, which is consistent with the dip observed in the active layer absorbance for a simulated ITO-based device. The electric field oscillations observed in the spectral range of 515−600 nm result from transmitted long-wavelength light penetrating the active layer and being reflected by the top Al electrode.[39−42] At all three $x-y$ points evaluated for the Al-NHA-based device, the electric field intensity in the lower portion of the device is stronger than that in the ITO-based device, demonstrating the plasmonic enhancements provided to the local electric field intensity when metallic nanostructured films are incorporated in devices.

Performance of Organic UV Photodetectors with Al-NHAs as Transparent Conducting Electrodes. Al-NHAs were experimentally fabricated and integrated into the photodiode devices. While nanoimprint lithography has been used to successfully fabricate NHAs,[4,43] nanosphere lithography (NSL) has also been used to produce NHAs and proved a superior fabrication method for this work because of its cost-effectiveness, speed, and scalability.[43] The procedure is illustrated in Figure S4 along with SEM images resulting from each step. NSL inherently produces a hexagonal NHA with the pitch determined by the nanosphere diameter and the diameter controlled by the etch conditions. A critical step in NSL is the formation of a large area, close-packed monolayer of nanospheres, and many methods for achieving this have been reported, including directional rubbing,[44−46] convective dragging,[47] spin-coating,[48] drop-coating,[49−51] and the air−water interface method.[52−59]

In this work, the monolayer of 200 nm diameter nanospheres was formed via drop-coating. After deposition, the monolayer was exposed to an oxygen plasma to shrink the spheres and create space between them. Ideally, this etching step will shrink the spheres minimally, just enough to create clean separation with no material between spheres, so that the eventual nanoholes will be separated by thin, continuous Al walls. The etch step is highly sensitive to etch power, time, and the flow rate ratio of the two process gases O_2 and Ar. The optimization of the etch conditions is summarized in Figure S5. After etching, 30 nm of Al was deposited via thermal evaporation onto the nanosphere monolayers with the impinging beam normal to the substrate to ensure that Al on top of the spheres remains physically separated from Al on the glass between the spheres, so that liftoff of spheres to generate nanoholes can be achieved. The SEM image in Figure S4 corresponding to this step was taken at the edge of a patterned area, with a higher magnification and a 40° tilt, to clearly demonstrate that this deposition has been achieved. Finally, toluene was used as a solvent to achieve chemical liftoff[57,58,60,61] by dissolving the spheres, resulting in the desired Al-NHA with a thickness of 30 nm.

The fabricated Al-NHAs were then evaluated as electrodes for device incorporation. For a transparent conducting electrode, optical transmittance will directly affect the device photoresponse strength. The transmittance of ITO and Al-NHA electrodes was measured and is shown in Figure 3a. The transmittance of the Al-NHA electrode does not exceed 40% throughout the entire tested spectral range, peaking at 36.8% under 380 nm illumination. The ITO electrode has around 90% transmittance in the range 380−600 nm, but the transmittance is lower, between 30 and 90%, in the range 300−380 nm. Another critical characteristic of a transparent conducting electrode is its sheet resistance, which will prevent the film from functioning as an electrode if the sheet resistance is too high. The sheet resistance for an Al-NHA electrode was measured to be 3.4 Ω sq^{-1} by using the four-point probe method. ITO electrodes, with a thickness of 200 nm, had a measured sheet resistance of 8.9 Ω sq^{-1}.

Devices were fabricated with a structure of Al-NHA (30 nm) or ITO (200 nm)/PEDOT:PSS (40 nm)/F8T2:$PC_{71}BM$ (350 nm, 100:4 weight ratio)/LiF(0.8 nm)/Al (100 nm) and evaluated. The dark current in Al-NHA-based devices is significantly reduced compared to ITO-based devices, as shown in Figure 3b. The dark current density (J_D) values produced by Al-NHA- and ITO-based devices are 4.4×10^{-7} and 8.3×10^{-5} mA cm^{-2}, respectively, under a −2 V bias, and 9.2×10^{-8} and 5.2×10^{-4} mA cm^{-2}, respectively, under a 2 V bias. Low J_D values typically correspond to more sensitive photoresponse and are therefore a desirable attribute of Al-NHA-based devices.

The external quantum efficiency (EQE) spectra of the Al-NHA- and ITO-based devices under 0, −1, and −2 V reverse biases are provided in Figure 3c. EQE represents the ratio of collected charge carriers to incident photons, providing a measure of photoresponse strength. Peaks around 350 and 515 nm, corresponding to the edges of the active layer absorbance peak, are produced by both Al-NHA- and ITO-based devices. Light with these wavelengths is absorbed weakly, so it penetrates the active layer and is absorbed in the top portion, enabling it to contribute significantly to reverse-bias photoresponse, the mechanism of which will be discussed in detail later. This is true for both Al-NHA- and ITO-based devices and agrees with the simulated electric field distributions presented in Figure 2b−e, where the electric field at the top of the active layer is most intense for incident light with wavelengths at the edges of the active layer absorbance peak. Notably, Al-NHA-based devices produce photoresponse that is more UV-selective than the ITO-based devices, as demonstrated by two spectral features. First, the UV-peak is slightly blue-shifted for Al-NHA-based devices, occurring at 350 nm instead of 360 nm as it does for ITO-based devices. This agrees with the simulated active layer absorbance shown in Figure 2a, where UV-peaks produced by Al-NHA-based devices were also blue-shifted from that of ITO-based devices. The other feature demonstrating the superior UV-selectivity of Al-NHA-based devices is the relative magnitude of EQE peaks. Under −2 V bias, Al-NHA-based devices produce a UV-peak that is slightly higher than the 515 nm peak, while ITO-based devices

DOI: 10.1021/acsanm.9b00902
ACS Appl. Nano Mater. 2019, 2, 4942−4953

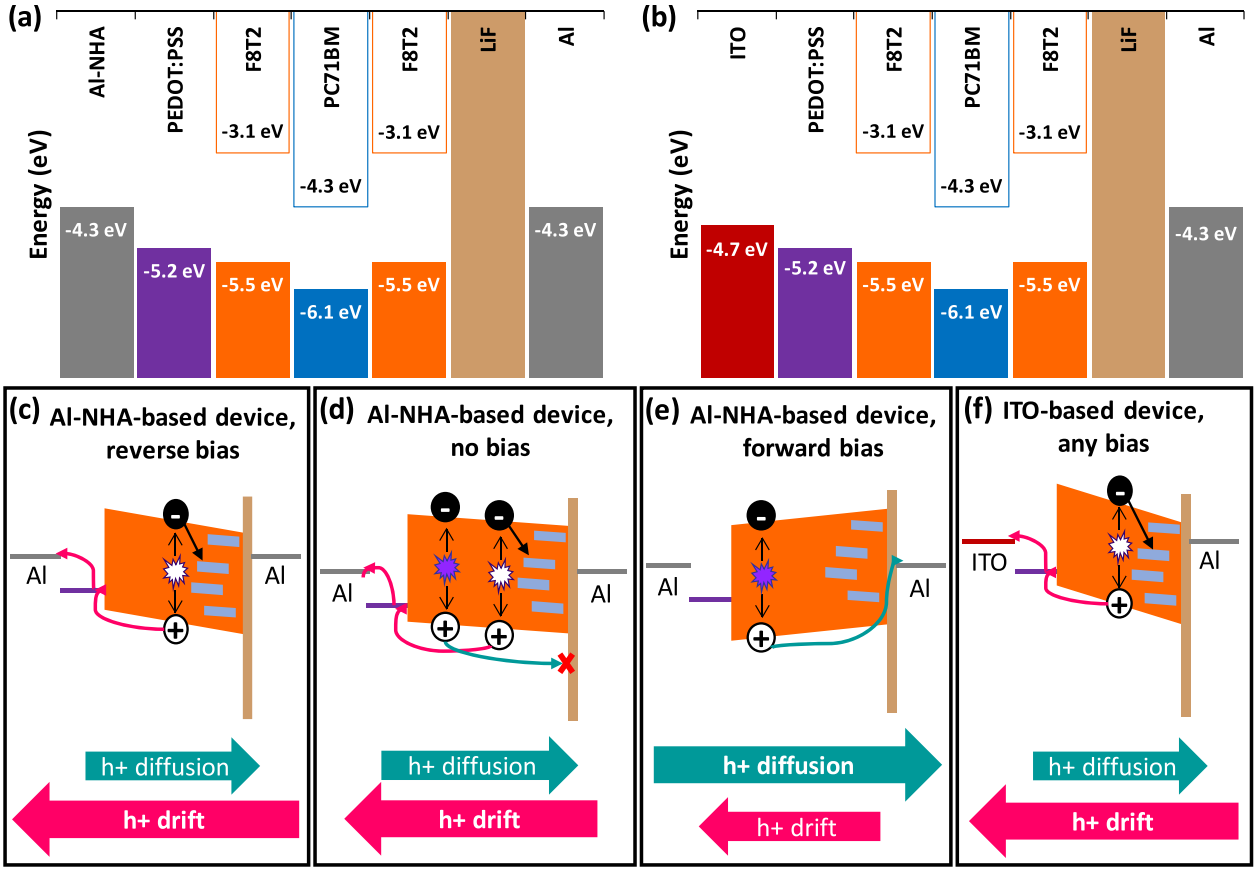

Figure 4. (a, b) Energy band diagrams for Al-NHA- and ITO-based devices. (c–e) Illustrations of response mechanism for an Al-NHA-based device under (c) applied reverse bias, (d) no applied bias, and (e) applied forward bias. (f) Illustration of response mechanism for an ITO-based device under any bias.

produce a UV-peak that is slightly lower than the 515 nm peak. The superior UV-selectivity exhibited by the Al-NHA-based devices could be due to the relatively high transmittance between 350 and 400 nm produced by the Al-NHA electrode (Figure 3a). The lower photoresponse strength produced by Al-NHA-based devices compared to ITO-based-devices, which is confirmed by the photocurrent densities (J_{PH}) produced under 360 nm illumination (Figure S6), is attributed to the lower optical transmittance of Al-NHA electrodes compared to ITO (Figure 3a).

For applications where photoresponse sensitivity is more important than strength, the specific detectivity (D^*) is a more meaningful figure of merit than EQE, as it accounts for the energy of incident photons at different wavelengths, the device active area, and the noise current in the device. The noise currents, calculated by a fast Fourier transform of the dark current measured against time[39,40,62] and shown in Table S1, are lower for Al-NHA-based devices than for ITO-based devices, enabling Al-NHA-based devices to produce competitive D^* values, shown in Figure 3d, despite their relatively weak photoresponse. The D^* values obtained from Al-NHA- and ITO-based devices without any applied bias are very similar, with the Al-NHA- and ITO-based devices producing peaks at 2.0×10^8 and 2.8×10^8 jones, respectively, under 340 nm illumination. Under applied reverse biases ITO-based devices achieve higher D^* values than Al-NHA-based devices, but they are within an order of magnitude. Additionally, Al-NHA-based devices have a UV-peak that is slightly blue-shifted from the UV-peak produced by the ITO-based-device. Under a −2 V bias, Al-NHA- and ITO-based devices produce respective D^* values of 4.0×10^9 and 1.2×10^{10} jones under 340 and 350 nm illumination, respectively. ITO can therefore be replaced with an Al-NHA electrode, which utilizes a cheaper, potentially flexible material, without significantly diminishing reverse-bias device performance.

Under forward bias, Al-NHA-based devices produce superior photoresponse compared to ITO-based devices, as evaluated by response strength, stability, and sensitivity and demonstrated in Figure 3e. Al-NHA-based devices show a new, distinct spectral shape, exhibiting one broad peak that corresponds to the absorption of the active layer and increases in magnitude for increasing forward biases. A maximum EQE value of 0.069% under 450 nm illumination and a 2 V bias is obtained. Contrarily, the EQE values produced by ITO-based devices decrease with increasing forward bias, while maintaining the same spectral shape as is produced under reverse bias. When the bias was increased from 0 to 0.5 V, the peak EQE value obtained under 350 nm illumination dropped from 0.053% to 0.023%. Increasing the forward bias to 1 V resulted in further reduced and unstable photoresponse. Because of both stronger EQE and lower dark (and noise) currents, Al-NHA-based devices produce superior D^* values under forward bias compared to the ITO-based devices, as shown in Figure 3f. Under a small forward bias of 0.5 V, the spectral shape produced by the Al-NHA-based device can be clearly observed and will be discussed later within the context of the general photoresponse mechanism, and the D^* values produced by the ITO-based device increased compared to the D^* values

DOI: 10.1021/acsanm.9b00902
ACS Appl. Nano Mater. 2019, 2, 4942−4953

produced without any bias. Detectivity values could not be obtained at higher biases from ITO-based devices because instability prevented the reliable calculation of noise current. As the forward bias applied to Al-NHA-based devices was increased, the D^* values produced also increased, peaking at 8.8×10^9 jones under 450 nm illumination and a 2 V bias. While the photoresponse values reported here are not among the strongest reported throughout the literature,[20−22] the novel bias-dependent response switching introduced in these Al-NHA-based devices is a significant achievement and could be applied to other systems to achieve photoresponse that is both strong and can be tuned by the bias applied.

Investigation of the Bias-Dependent Photoresponse Mechanism. The bias-dependent response switching achieved by the Al-NHA-based device is hypothesized to be related to electrode symmetry. Response switching has also been shown for a device with a structure of Al/P3HT:PC_{71}BM/Al, which produced two-peak EQE spectra under reverse bias and one-peak spectra under forward bias, corresponding to the edges and peak of the active layer absorbance, respectively.[63] The electrode symmetry allowed the assignment of cathode and anode to be determined by the applied bias, rather than the electrode material, thus enabling bias-dependent response switching.[63] Figures 4a and 4b show band level diagrams for Al-NHA- and ITO-based devices, respectively, demonstrating the electrode symmetry introduced by the Al-NHA electrode. It should be noted that due to the conventional device structure, the interfacial layers remain asymmetric and so does the overall device. The proposed mechanism of the bias-dependent response switching is illustrated in Figure 4c−f, which provides schematic representations of the dominant photoresponse mechanisms for Al-NHA-based devices under reverse bias (Figure 4c), no bias (Figure 4d), and forward bias (Figure 4e) and for ITO-based devices under any bias (Figure 4f). For each case, a band diagram is drawn and includes the relevant band tilting and charge carrier flow. Arrows indicate the direction and relative strength of hole drift (denoted as h+ drift) and hole diffusion (denoted as h+ diffusion) currents. Generally, light absorption occurring in the top and bottom of the active layer, denoted with white and purple stars, respectively, is hypothesized to correspond to hole drift and diffusion, respectively.

For Al-NHA-based devices, the spectral shape of the photoresponse depends on the bias applied. Under reverse bias (Figure 4c), the energy bands tilt to provide a driving force for hole drift. Light absorbed at the top of the active layer contributes most significantly to photoresponse, since photogenerated holes can successfully drift downward to be collected at the bottom Al-NHA electrode (anode). Peak photoresponse is therefore achieved at the edges of the F8T2 absorption peak, around 350 and 515 nm, since these wavelengths can penetrate the active layer and be absorbed near the top of the layer. Light within the absorption peak is absorbed strongly in the bottom portion of the active layer and generates excitons there.[33] An applied reverse bias does not provide any driving force for photogenerated holes in the bottom of the active layer to diffuse upward in the active layer, so a space charge region is established and suppresses the photoresponse for light absorbed in this region.[40]

An Al-NHA-based device without any applied bias is also dominated by hole drift, as illustrated in Figure 4d and evidenced by the spectral shape observed in Figure 3c−f. The drift-dominated photoresponse in this case is attributed to the presence of the LiF layer, which has two significant effects. First, LiF has hole-blocking capabilities, so it prevents any holes diffusing upward through the active layer from being collected at the top Al cathode and contributing to photoresponse.[33,63] Second, the presence of LiF has been shown to make the Al work function slightly less negative,[64] resulting in a device that does not truly have symmetric electrodes but instead has a small built-in reverse bias, which provides a driving force for hole drift to dominate over diffusion, as it does under an applied reverse bias.

An applied forward bias enables the Al-NHA-based devices to produce spectrally distinct, diffusion-dominated photoresponse by effectively inverting the device, as illustrated in Figure 4e. In this case, the applied bias can overcome the built-in reverse bias introduced by the LiF layer and tilt the bands forward, providing a driving force for hole diffusion instead of drift. Light absorbed in the lower portion of the active layer, in the spectral range corresponding to the active layer absorption peak between about 350 and 515 nm, contributes most significantly to photoresponse in this case. The applied forward bias provides a driving force for photogenerated holes in the lower portion of the active layer to diffuse upward through the layer, rather than form a response-suppressing space charge region. Beyond aiding the upward diffusion of holes, this driving force also enables them to overcome the hole-blocking property of LiF and be collected at the top Al electrode. In addition, the forward bias provides some resistance to hole drift, suppressing photoresponse at 350 and 515 nm and resulting in diffusion-dominated photoresponse spectra with a single peak around 450 nm.

For an ITO-based device, the asymmetry of the electrode work functions causes the bands to tilt and create a built-in reverse bias, as illustrated in Figure 4f, resulting in behavior similar to that of an Al-NHA-based device under applied reverse bias (Figure 4c). Because the built-in bias acts as a reverse bias, applying an additional reverse bias improves the photoresponse strength while applying a forward bias diminishes it (Figures 3c and 3e, respectively). Two-peak photoresponse spectra are always produced regardless of the bias applied because the built-in reverse bias, resulting from the asymmetry of the electrode work functions, suppresses hole diffusion. Contrary to the response switching achieved in Al-NHA-based devices, the ITO-based device is locked in to a drift-dominated photoresponse, and any hole diffusion that occurs is blocked from contributing to the photoresponse by both the LiF hole blocking layer and the built-in reverse bias. Likewise, devices with a structure of ITO/poly[9,9-bis(60-(*N*,*N*-diethylamino)propyl)fluorene-*alt*-9,9-bis(3-ethyl-(oxetane-3-ethyloxy)hexyl)fluorene] (PFN-OX)/P3HT:PC_{71}BM/Al were reported to produce spectrally similar photoresponse under both reverse and forward biases.[41] Even under a strong forward bias of 60 V, ITO-based devices produced EQE spectra with two peaks corresponding to the edges of the active layer absorbance.[41] In our case, ITO-based devices produce weak, unstable photoresponse under applied forward biases, whereas Al-NHA-based devices produce strong, stable photoresponse. Al-NHA electrodes enable distinct behavior simply by changing the bias applied to a device, effectively producing two devices in one.

The response mechanism described in Figure 4 can be used to further explain some of the results presented in Figure 3. Figure 3b demonstrates that the dark current produced by Al-NHA-based devices is significantly lower than that produced

DOI: 10.1021/acsanm.9b00902
ACS Appl. Nano Mater. 2019, 2, 4942−4953

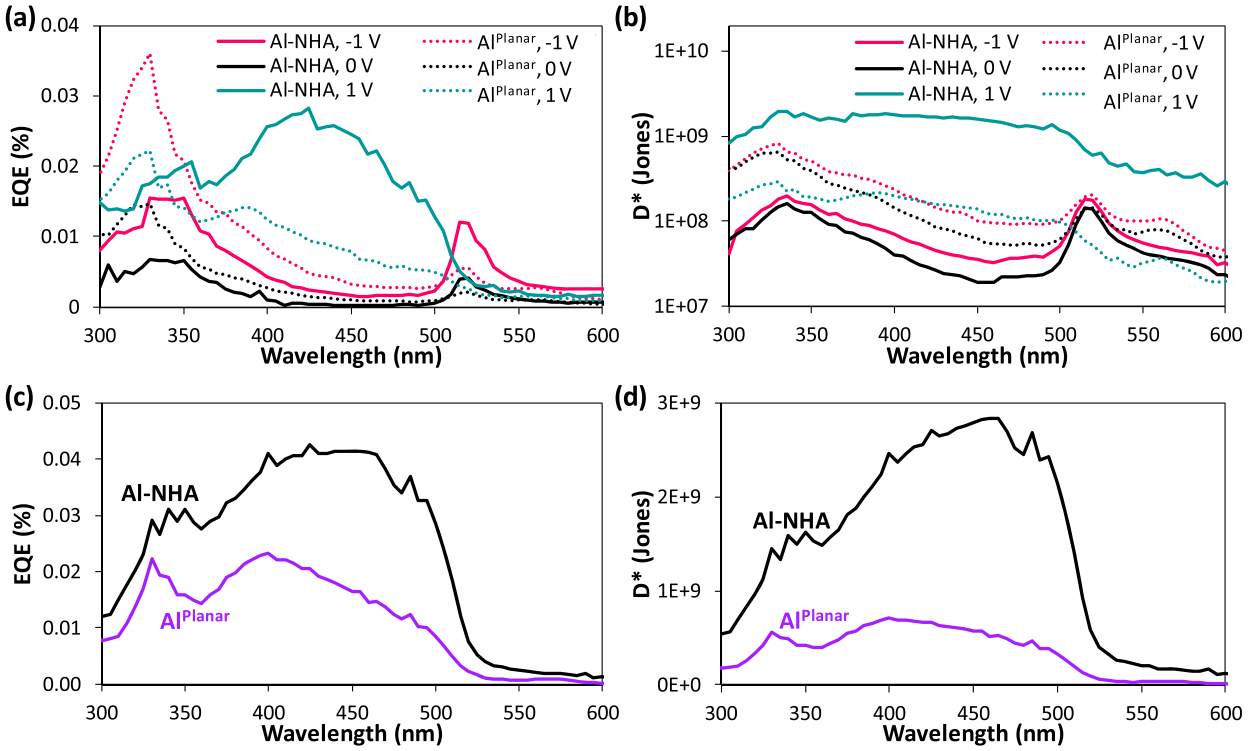

Figure 5. (a) EQE and (b) D^* spectra for Al-NHA- and Al^{Planar}-based conventional devices. (c) EQE and (d) D^* spectra for Al-NHA- and Al^{Planar}-based hole-only devices with the structure of Al-NHA or Al^{Planar}/PEDOT:PSS/F8T2:$PC_{71}BM$/MoO_3/Al under no applied bias.

by ITO-based devices, which can be attributed to two factors. First, as shown in Figure 4a,b, the hole injection barrier from Al into PEDOT:PSS (0.9 eV) is higher than the injection barrier from ITO into PEDOT:PSS (0.5 eV), resulting in lower dark current in Al-NHA-based devices under forward bias. Second, the built-in reverse bias is weaker in Al-NHA-based devices than in ITO-based devices due to the significant asymmetry between the ITO and Al work functions, yielding a stronger driving force for hole drift in ITO-based devices and a subsequently higher dark current. The stronger built-in reverse bias and resulting drift driving force in ITO-based devices, compared to Al-NHA-based devices, likely also contribute to the superior reverse-bias photoresponse achieved by ITO-based devices (Figure 3c).

The photoresponse of Al-NHA-based devices under the small applied forward bias of 0.5 V illustrates the transition between drift-dominated to diffusion-dominated photoresponse described in Figure 4. Its spectral shape, which can be clearly observed in Figure 3f, has three peaks centered around 350, 450, and 515 nm. The 350 and 515 nm peaks correspond to the drift-based behavior produced under reverse or no bias, while the 450 nm peak corresponds to the diffusion-based behavior produced under forward bias. The small forward bias of 0.5 V does not provide enough resistance to hole drift to prevent light absorbed at the top of the active layer from contributing to photoresponse, resulting in the peaks at 350 and 515 nm, but does provide a sufficient driving force for diffusion-based photoresponse to occur, resulting in the peak at 450 nm. Therefore, both drift- and diffusion-based response mechanisms are possible at this small forward bias.

Confirmation of the Photoresponse Mechanism and the Impact of Plasmonic Al-NHAs. Devices based on 10 nm planar Al electrodes (denoted as Al^{Planar}, having a measured sheet resistance of 7.3 Ω sq^{-1}) and devices with a hole-only architecture based on both Al^{Planar} and Al-NHA electrodes were investigated to confirm the proposed photoresponse mechanism and to isolate the impact of the Al-NHA induced plasmonic effects from the effects of the electrode material. To make a full electrode comparison, an Al^{Planar}-based device was also simulated and evaluated (Figure S7). The Al^{Planar}-based device produces a weaker and slightly blue-shifted active layer absorbance compared to both the Al-NHA- and ITO-based devices (Figure S7a), which is attributed to the low transmittance and slightly blue-shifted peak transmittance of fabricated 10 nm Al thin films (Figure S7b). The internal electric field distributions (Figure S7c) clearly show that the incorporation of the NHA provides an electric field enhancement, as the Al^{Planar}-based device produces the weakest internal electric field intensities throughout the device. Stronger intensities are produced within the glass substrate because the reflectance of the Al^{Planar} electrode is much higher than the Al-NHA or ITO electrodes (Figure S7d), but electric field intensity within the substrate has no impact on device performance. The dark and photocurrent densities produced by Al^{Planar}-based devices are provided in Figure S7e.

Al^{Planar}-based devices produce two EQE peaks that are similar, but slightly blue-shifted, compared to those of Al-NHA-based devices under a 0 or −1 V bias, as shown in Figure 5a. Notably, when the electrode is changed from ITO to Al-NHA and then to Al^{Planar}, the UV-peak blue-shifts and grows in magnitude relative to the peak at 515 nm. This phenomenon is summarized in Table S2 and is attributed to a combined effect of the electrode transmittance (Figure S7b) and the penetration depth of light into the active layer (Figure S8). As the wavelength of incident light increases within the UV spectral range, the transmittance increases while the penetration depth decreases. Both factors are directly proportional to photoresponse strength, so the trade-off between the two

DOI: 10.1021/acsanm.9b00902
ACS Appl. Nano Mater. 2019, 2, 4942−4953

determines the position of the UV peak. For electrodes with decreased transmittance, like the Al^{Planar} electrode, the penetration depth becomes the primary determinant of peak position, and the UV peak blue-shifts.

Under 1 V forward bias, Al^{Planar}-based devices produce an EQE peak at 330 nm and a second peak around 390 nm which decreases throughout the spectral range between about 400 and 500 nm before it cuts off at 515 nm (Figure 5a). This photoresponse is distinct from and inferior to the strong peak produced by the Al-NHA-based device under forward bias that clearly corresponds to the active layer absorption. The enhancement provided to the electric field intensity by the Al-NHA electrode is hypothesized to act as a small forward bias within the device, pushing the Al-NHA-based device toward diffusion-dominated behavior while the Al^{Planar}-based device produces drift- and diffusion-based photoresponse peaks with similar magnitudes. D^* spectra for Al-NHA- and Al^{Planar}-based devices are shown in Figure 5b and show the same trends.

To further confirm the proposed photoresponse mechanism, hole-only devices were fabricated by replacing the hole-blocking LiF layer with a hole-transporting MoO_3 layer.[65] Without the hole-blocking and built-in bias resulting from the LiF layer, true electrode symmetry and overall device symmetry were achieved, and the Al-NHA- and Al^{Planar}-based devices produce diffusion-dominated photoresponse without any applied bias. It is reasonable that hole diffusion would dominate over drift without any applied or internal bias, since light corresponding to diffusion-based response is absorbed more strongly than that corresponding to drift-based response. In addition, the Al-NHA-based device should produce stronger photoresponse since plasmonic enhancements to the electric field intensity should improve the hole diffusion driving force. Indeed, as shown in Figure 5c,d, the Al-NHA-based devices exhibit stronger EQE and D^* values, with spectra that are clearly dominated by hole diffusion, compared to those of Al^{Planar}-based devices, which are weaker and are similarly affected by hole drift and diffusion. The comparison of Al-NHA- and Al^{Planar}-based devices shown in Figure 5 indicates that Al-NHA electrodes positively impact forward-bias photoresponse through plasmonic enhancements to the internal electric field, as Al-NHA-based devices outperform both Al^{Planar}- and ITO-based devices when evaluated for response strength and stability.

The response speeds of Al-NHA-, Al^{Planar}-, and ITO-based devices were tested under 360 nm illumination and 1 and −1 V biases (Figures 6a and 6b, respectively), further indicating that device performance benefits from plasmonic enhancements to the internal electric field of Al-NHA-based devices. The wavelength of 360 nm was chosen because all devices generate photoresponse at that wavelength under both forward and reverse biases, and it is within the spectral range where plasmonic enhancements are expected. The rise (and fall) times were 0.35 s (0.49 s) and 0.45 s (0.51 s) under 1 V bias for the Al-NHA- and Al−P^{lanar}-based devices, respectively. The faster photoresponse speed of the Al-NHA-based devices indicates that the devices benefit from plasmonic enhancements to the internal electric field intensity, which acts as a small forward bias and improves diffusion-based photoresponse resulting from light absorbed in the lower portion of the active layer. In Figure 6b, the response speeds of all three devices are compared under −1 V bias. The rise (fall) times are 0.37 s (0.39 s), 0.42 s (0.45 s), and 0.3 s (0.44 s) for the Al-NHA-, Al−P^{lanar}-, and ITO-based devices, respectively. Under reverse bias, the Al-NHA-based devices undergo drift-dominated photoresponse and rely on light absorption in the top of the active layer, so plasmonic enhancements to the electric field are not relevant to the response speed.

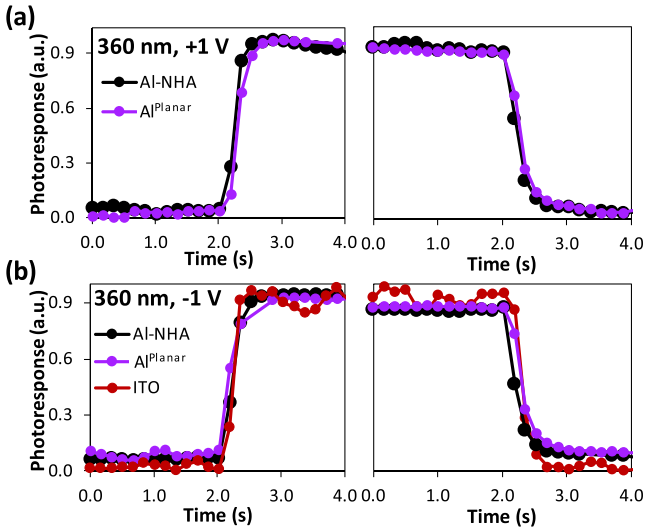

Figure 6. Response speed under 360 nm illumination for (a) Al-NHA- and Al^{Planar}-based devices at 1 V bias and (b) Al-NHA-, Al^{Planar}-, and ITO-based devices at −1 V bias.

CONCLUSIONS

Plasmonic Al-NHA electrodes have been designed by 3D-FDTD simulations, fabricated by nanosphere lithography, and incorporated as transparent conducting electrodes in organic ultraviolet photodetectors. The hexagonal Al-NHA with a diameter and pitch of 175 and 200 nm, respectively, exhibits both strong UV-selective active layer absorbance and enhanced internal electric field intensity from 3D-FDTD simulations. This plasmonic-enhanced internal electric field increases the driving force for hole diffusion, resulting in bias-dependent response switching. The Al-NHA-based devices produce two narrow photoresponse peaks with D^* values of 4.0×10^9 and 4.6×10^9 jones under 340 and 515 nm illumination, respectively, and −2 V bias and one broad photoresponse peak with a peak D^* of 8.8×10^9 jones under 450 nm illumination and 2 V bias, demonstrating spectral photoresponse that is similar under reverse bias and superior under forward bias compared to ITO-based control devices. The EQE values produced by these devices are relatively low, but the mechanisms investigated and demonstrated in this work could be applied to other systems. With different active materials, such as perovskites and other polymers, stronger photoresponse could be produced while the novel bias-dependent response-switching enabled by Al-NHA electrodes is also achieved. The ability to tune the spectral photoresponse of devices by applying either reverse or forward bias improves device applicability, making Al-NHA electrodes a promising option for ITO-free organic UV photodetectors with improved photoresponse and bias-dependent response tunability.

ASSOCIATED CONTENT

Supporting Information

The Supporting Information is available free of charge on the ACS Publications website at DOI: 10.1021/acsanm.9b00902.

DOI: 10.1021/acsanm.9b00902
ACS Appl. Nano Mater. 2019, 2, 4942−4953

Supplementary text, Figures S1−S8, and Tables S1 and S2 (PDF)

AUTHOR INFORMATION

Corresponding Author

*E-mail: qyu@uw.edu.

ORCID

Monica R. Esopi: 0000-0003-2262-4802

Qiuming Yu: 0000-0002-2401-4664

Notes

The authors declare no competing financial interest.

ACKNOWLEDGMENTS

The authors gratefully acknowledge financial support provided by the Defense Threat Reduction Agency (HDTRA1-15-1-0021) and the National Science Foundation (CMMI 1661660). Part of this work was conducted at the Washington Nanofabrication Facility/Molecular Analysis Facility, a National Nanotechnology Coordinated Infrastructure (NNCI) site at the University of Washington, which is supported in part by funds from the National Science Foundation (Awards NNCI-1542101, 1337840, and 0335765), the National Institutes of Health, the Molecular Engineering & Sciences Institute, the Clean Energy Institute, the Washington Research Foundation, the M. J. Murdock Charitable Trust, Altatech, ClassOne Technology, GCE Market, Google, and SPTS. Part of this work was conducted at the Washington Clean Energy Testbeds, a facility operated by the University of Washington Clean Energy Institute. M.R.E. acknowledges a fellowship from the University of Washington Clean Energy Institute. Some device fabrication and characterization steps were performed in the University of Washington Department of Chemistry's Photonics Research Center. UV−vis absorption was conducted in the lab of Professor Samson Jenekhe.

REFERENCES

(1) Brongersma, M. L. Plasmonic Photodetectors, Photovoltaics, and Hot-Electron Devices. *Proc. IEEE* **2016**, *104* (12), 2349−2361.

(2) Schuller, J. A.; Barnard, E. S.; Cai, W. S.; Jun, Y. C.; White, J. S.; Brongersma, M. L. Plasmonics for extreme light concentration and manipulation. *Nat. Mater.* **2010**, *9* (3), 193−204.

(3) Berini, P. Surface plasmon photodetectors and their applications. *Laser & Photonics Reviews* **2014**, *8* (2), 197−220.

(4) Richardson, B. J.; Zhu, L.; Yu, Q. M. Design and development of plasmonic nanostructured electrodes for ITO-free organic photovoltaic cells on rigid and highly flexible substrates. *Nanotechnology* **2017**, *28*, 165401.

(5) Arredondo, B.; de Dios, C.; Vergaz, R.; Criado, A. R.; Romero, B.; Zimmermann, B.; Wurfel, U. Performance of ITO-free inverted organic bulk heterojunction photodetectors: Comparison with standard device architecture. *Org. Electron.* **2013**, *14* (10), 2484−2490.

(6) Atwater, H. A.; Polman, A. Plasmonics for improved photovoltaic devices. *Nat. Mater.* **2010**, *9* (3), 205−213.

(7) Barnes, W. L.; Dereux, A.; Ebbesen, T. W. Surface plasmon subwavelength optics. *Nature* **2003**, *424* (6950), 824−830.

(8) Genet, C.; Ebbesen, T. W. Light in tiny holes. *Nature* **2007**, *445* (7123), 39−46.

(9) Chang, S. H.; Gray, S. K.; Schatz, G. C. Surface plasmon generation and light transmission by isolated nanoholes and arrays of nanoholes in thin metal films. *Opt. Express* **2005**, *13* (8), 3150−3165.

(10) Zhang, J. X.; Zhang, L. D.; Xu, W. Surface plasmon polaritons: physics and applications. *J. Phys. D: Appl. Phys.* **2012**, *45* (11), 113001.

(11) Razeghi, M.; Rogalski, A. Semiconductor ultraviolet detectors. *J. Appl. Phys.* **1996**, *79* (10), 7433−7473.

(12) Kedadra, A.; Traiche, M. Photomultiplier and avalanche photodiode detection performance for LiDAR application to environment studies. *J. Appl. Remote Sens.* **2014**, *8* (1), 083568.

(13) Gurin, N. T.; Novikov, S. G.; Korneev, I. V.; Shtan'ko, A. A.; Rodionov, V. A. Position-sensitive photodetector for rotation-angle transducers. *Technol. Phys. Lett.* **2011**, *37* (3), 271−273.

(14) Bhattacharya, P. *Semiconductor Optoelectronic Devices*; Prentice Hall: 1996.

(15) Kasap, S. O. *Principles of Electronic Materials and Devices*; McGraw-Hill: New York, 2006.

(16) Baeg, K. J.; Binda, M.; Natali, D.; Caironi, M.; Noh, Y. Y. Organic Light Detectors: Photodiodes and Phototransistors. *Adv. Mater.* **2013**, *25* (31), 4267−4295.

(17) Liu, Y.; Lang, F.; Dittrich, T.; Steigert, A.; Fischer, C. H.; Kohler, T.; Plate, P.; Rappich, J.; Lux-Steiner, M. C.; Schmid, M. Enhancement of photocurrent in an ultra-thin perovskite solar cell by Ag nanoparticles deposited at low temperature. *RSC Adv.* **2017**, *7* (3), 1206−1214.

(18) Lan, W. X.; Wang, Y. W.; Singh, J.; Zhu, F. R. Omnidirectional and Broadband Light Absorption Enhancement in 2-D Photonic-Structured Organic Solar Cells. *ACS Photonics* **2018**, *5* (3), 1144−1150.

(19) Salomon, L.; Grillot, F.; Zayats, A. V.; de Fornel, F. Near-field distribution of optical transmission of periodic subwavelength holes in a metal film. *Phys. Rev. Lett.* **2001**, *86* (6), 1110−1113.

(20) Wang, H.; Haroldson, R.; Balachandran, B.; Zakhidov, A.; Sohal, S.; Chan, J. Y.; Zakhidov, A.; Hu, W. Nanoimprinted Perovskite Nanograting Photodetector with Improved Efficiency. *ACS Nano* **2016**, *10* (12), 10921−10928.

(21) Du, B. W.; Yang, W. Q.; Jiang, Q.; Shan, H. Y.; Luo, D. Y.; Li, B. W.; Tang, W. C.; Lin, F.; Shen, B.; Gong, Q. H.; Zhu, X.; Zhu, R.; Fang, Z. Y. Plasmonic-Functionalized Broadband Perovskite Photodetector. *Adv. Opt. Mater.* **2018**, *6* (8), 1701271.

(22) Luo, X.; Du, L. L.; Wen, Z. W.; Lv, W. L.; Zhao, F. Y.; Jiang, X. Y.; Peng, Y. Q.; Sun, L.; Li, Y.; Rao, J. W. Remarkably enhanced red-NIR broad spectral absorption via gold nanoparticles: applications for organic photosensitive diodes. *Nanoscale* **2015**, *7* (34), 14422−14433.

(23) Hou, J. L.; Fischer, A.; Yang, S. C.; Benduhn, J.; Widmer, J.; Kasemann, D.; Vandewal, K.; Leo, K. Plasmon-Induced Sub-Bandgap Photodetection with Organic Schottky Diodes. *Adv. Funct. Mater.* **2016**, *26* (31), 5741−5747.

(24) Knight, M. W.; King, N. S.; Liu, L. F.; Everitt, H. O.; Nordlander, P.; Halas, N. J. Aluminum for Plasmonics. *ACS Nano* **2014**, *8* (1), 834−840.

(25) Gong, T.; Munday, J. N. Aluminum-based hot carrier plasmonics. *Appl. Phys. Lett.* **2017**, *110* (2), 021117.

(26) Boltasseva, A.; Atwater, H. A. Low-Loss Plasmonic Metamaterials. *Science* **2011**, *331* (6015), 290−291.

(27) Cheng, C. W.; Liao, Y. J.; Liu, C. Y.; Wu, B. H.; Raja, S. S.; Wang, C. Y.; Li, X. Q.; Shih, C. K.; Chen, L. J.; Gwo, S. Epitaxial Aluminum-on-Sapphire Films as a Plasmonic Material Platform for Ultraviolet and Full Visible Spectral Regions. *ACS Photonics* **2018**, *5* (7), 2624−2630.

(28) Zhu, A. Y.; Kuznetsov, A. I.; Luk'yanchuk, B.; Engheta, N.; Genevet, P. Traditional and emerging materials for optical metasurfaces. *Nanophotonics* **2017**, *6* (2), 452−471.

(29) Ding, G.; Deng, J.; Zhou, L.; Gan, Q.; Hwang, J. C. M.; Dierolf, V.; Bartoli, F. J.; Mazuir, C.; Schoenfeld, W. V. Al nanogrid electrode for ultraviolet detectors. *Opt. Lett.* **2011**, *36* (18), 3663−3665.

(30) Taguchi, A.; Saito, Y.; Watanabe, K.; Yijian, S.; Kawata, S. Tailoring plasmon resonances in the deep-ultraviolet by size-tunable fabrication of aluminum nanostructures. *Appl. Phys. Lett.* **2012**, *101* (8), 081110.

(31) Du, Q. G.; Ren, H.; Wu, L.; Bai, P.; Png, C. E.; Sun, X. W.; Kam, C. H.; de Sterke, C. M. Light absorption mechanism in organic solar cells with hexagonal lattice nanohole aluminum transparent electrodes. *J. Opt.* **2015**, *17* (8), 085901.

DOI: 10.1021/acsanm.9b00902
ACS Appl. Nano Mater. 2019, 2, 4942−4953

(32) Zheng, B. Y.; Wang, Y. M.; Nordlander, P.; Halas, N. J. Color-Selective and CMOS-Compatible Photodetection Based on Aluminum Plasmonics. *Adv. Mater.* **2014**, *26* (36), 6318−6323.
(33) Esopi, M. R.; Calcagno, M.; Yu, Q. M. Organic Ultraviolet Photodetectors Exhibiting Photomultiplication, Low Dark Current, and High Stability. *Advanced Materials Technologies* **2017**, *2* (8), 1700025.
(34) Lumerical, Inc., Material Database (Optical). https://kb.lumerical.com/en/materials_material_database_optical.html.
(35) Li, H. H. Refractive index of alkali halides and its wavelength and temperature derivatives. *J. Phys. Chem. Ref. Data* **1976**, *5*, 329.
(36) RefractiveIndex.INFO Optical Constants of Lithium Fluoride (LiF). https://refractiveindex.info/?shelf=main&book=LiF&page=Li.
(37) Wang, B. M.; Ruud, C. J.; Price, J. S.; Kim, H.; Giebink, N. C. Graded-Index Fluoropolymer Antireflection Coatings for Invisible Plastic Optics. *Nano Lett.* **2019**, *19* (2), 787−792.
(38) Galvan, D. D.; Spackova, B.; Slaby, J.; Sun, F.; Ho, Y. H.; Homola, J.; Yu, Q. M. Surface-Enhanced Raman Scattering on Gold Nanohole Arrays in Symmetrical Dielectric Environments Exhibiting Electric Field Extension. *J. Phys. Chem. C* **2016**, *120* (44), 25519−25529.
(39) Esopi, M. R.; Zheng, E. J.; Zhang, X. Y.; Cai, C.; Yu, Q. M. Tuning the spectral response of ultraviolet organic-inorganic hybrid photodetectors via charge trapping and charge collection narrowing. *Phys. Chem. Chem. Phys.* **2018**, *20* (16), 11273−11284.
(40) Armin, A.; Jansen-van Vuuren, R. D.; Kopidakis, N.; Burn, P. L.; Meredith, P. Narrowband light detection via internal quantum efficiency manipulation of organic photodiodes. *Nat. Commun.* **2015**, *6*, 8.
(41) Miao, J. L.; Zhang, F. J.; Du, M. D.; Wang, W. B.; Fang, Y. Photomultiplication type narrowband organic photodetectors working at forward and reverse bias. *Phys. Chem. Chem. Phys.* **2017**, *19* (22), 14424−14430.
(42) Wang, W. B.; Zhang, F. J.; Du, M. D.; Li, L. L.; Zhang, M.; Wang, K.; Wang, Y. S.; Hu, B.; Fang, Y.; Huang, J. S. Highly Narrowband Photomultiplication Type Organic Photodetectors. *Nano Lett.* **2017**, *17* (3), 1995−2002.
(43) Xu, S. P.; Lei, Y. Template-Assisted Fabrication of Nanostructured Arrays for Sensing Applications. *ChemPlusChem.* **2018**, *83* (8), 741−755.
(44) Kim, Y.; Bicanic, K.; Tan, H. R.; Ouellette, O.; Sutherland, B. R.; de Arguer, F. P. G.; Jo, J. W.; Liu, M. X.; Sun, B.; Liu, M.; Hoogland, S.; Sargent, E. H. Nanoimprint-Transfer-Patterned Solids Enhance Light Absorption in Colloidal Quantum Dot Solar Cells. *Nano Lett.* **2017**, *17* (4), 2349−2353.
(45) Jang, D.; Kim, Y.; Kim, T. Y.; Koh, K.; Jeong, U.; Cho, J. Force-assembled triboelectric nanogenerator with high-humidity-resistant electricity generation using hierarchical surface morphology. *Nano Energy* **2016**, *20*, 283−293.
(46) Park, C.; Lee, T.; Xia, Y. N.; Shin, T. J.; Myoung, J.; Jeong, U. Quick, Large-Area Assembly of a Single-Crystal Monolayer of Spherical Particles by Unidirectional Rubbing. *Adv. Mater.* **2014**, *26* (27), 4633−4638.
(47) Prevo, B. G.; Velev, O. D. Controlled, rapid deposition of structured coatings from micro- and nanoparticle suspensions. *Langmuir* **2004**, *20* (6), 2099−2107.
(48) Choi, J. Y.; Alford, T. L.; Honsberg, C. B. Solvent-Controlled Spin-Coating Method for Large-Scale Area Deposition of Two-Dimensional Silica Nanosphere Assembled Layers. *Langmuir* **2014**, *30* (20), 5732−5738.
(49) Liu, J.; Chen, C. Y.; Yang, G. S.; Chen, Y. S.; Yang, C. F. Effect of the Fabrication Parameters of the Nanosphere Lithography Method on the Properties of the Deposited Au-Ag Nanoparticle Arrays. *Materials* **2017**, *10* (4), 381.
(50) Purwidyantri, A.; Chen, C. H.; Hwang, B. J.; Luo, J. D.; Chiou, C. C.; Tian, Y. C.; Lin, C. Y.; Cheng, C. H.; Lai, C. S. Spin-coated Au-nanohole arrays engineered by nanosphere lithography for a Staphylococcus aureus 16S rRNA electrochemical sensor. *Biosens. Bioelectron.* **2016**, *77*, 1086−1094.
(51) Mikac, L.; Ivanda, M.; Gotic, M.; Janicki, V.; Zorc, H.; Janci, T.; Vidacek, S. Surface-enhanced Raman spectroscopy substrate based on Ag-coated self-assembled polystyrene spheres. *J. Mol. Struct.* **2017**, *1146*, 530−535.
(52) Ingram, W. M.; Han, C. Q.; Zhang, Q. J.; Zhao, Y. P. Optimization of Ag-Coated Polystyrene Nanosphere Substrates for Quantitative Surface-Enhanced Raman Spectroscopy Analysis. *J. Phys. Chem. C* **2015**, *119* (49), 27639−27648.
(53) Weekes, S. M.; Ogrin, F. Y.; Murray, W. A.; Keatley, P. S. Macroscopic arrays of magnetic nanostructures from self-assembled nanosphere templates. *Langmuir* **2007**, *23* (3), 1057−1060.
(54) Sirotkin, E.; Apweiler, J. D.; Ogrin, F. Y. Macroscopic Ordering of Polystyrene Carboxylate-Modified Nanospheres Self-Assembled at the Water-Air Interface. *Langmuir* **2010**, *26* (13), 10677−10683.
(55) Stavroulakis, P. I.; Christou, N.; Bagnall, D. Improved deposition of large scale ordered nanosphere monolayers via liquid surface self-assembly. *Mater. Sci. Eng., B* **2009**, *165* (3), 186−189.
(56) He, Y. Z.; Larsen, G. K.; Ingram, W.; Zhao, Y. P. Tunable Three-Dimensional Helically Stacked Plasmonic Layers on Nanosphere Monolayers. *Nano Lett.* **2014**, *14* (4), 1976−1981.
(57) Chen, K.; Rajeeva, B. B.; Wu, Z. L.; Rukavina, M.; Dao, T. D.; Ishii, S.; Aono, M.; Nagao, T.; Zheng, Y. B. Moire Nanosphere Lithography. *ACS Nano* **2015**, *9* (6), 6031−6040.
(58) Wu, Z. L.; Chen, K.; Menz, R.; Nagao, T.; Zheng, Y. B. Tunable multiband metasurfaces by moire nanosphere lithography. *Nanoscale* **2015**, *7* (48), 20391−20396.
(59) Ho, C. C.; Chen, P. Y.; Lin, K. H.; Juan, W. T.; Lee, W. L. Fabrication of Monolayer of Polymer/Nanospheres Hybrid at a Water-Air Interface. *ACS Appl. Mater. Interfaces* **2011**, *3* (2), 204−208.
(60) Chong, M. A. S.; Zheng, Y. B.; Gao, H.; Tan, L. K. Combinational template-assisted fabrication of hierarchically ordered nanowire arrays on substrates for device applications. *Appl. Phys. Lett.* **2006**, *89* (23), 233104.
(61) Wu, Z. L.; Li, W.; Yogeesh, M. N.; Jung, S. Y.; Lee, A. L.; McNicholas, K.; Briggs, A.; Bank, S. R.; Belkin, M. A.; Akinwande, D.; Zheng, Y. B. Tunable Graphene Metasurfaces with Gradient Features by Self-Assembly-Based Moire Nanosphere Lithography. *Adv. Opt. Mater.* **2016**, *4* (12), 2035−2043.
(62) Xu, X. B.; Chueh, C. C.; Jing, P. F.; Yang, Z. B.; Shi, X. L.; Zhao, T.; Lin, L. Y.; Jen, A. K. Y. High-Performance Near-IR Photodetector Using Low-Bandgap MA(0.5)FA(0.5)Pb(0.5)Sn(0.5)-I(3) Perovskite. *Adv. Funct. Mater.* **2017**, *27* (28), 1701053.
(63) Li, L. L.; Zhang, F. J.; Wang, J.; An, Q. S.; Sun, Q. Q.; Wang, W. B.; Zhang, J.; Teng, F. Achieving EQE of 16,700% in P3HT: PC71BM based photodetectors by trap-assisted photomultiplication. *Sci. Rep.* **2015**, *5*, 9181.
(64) Kim, S.; Lee, J.; Dao, V. A.; Lee, S.; Balaji, N.; Ahn, S.; Hussain, S. Q.; Han, S.; Jung, J.; Jang, J.; Lee, Y.; Yi, J. Effects of LiF/Al back electrode on the amorphous/crystalline silicon heterojunction solar cells. *Mater. Sci. Eng., B* **2013**, *178* (9), 660−664.
(65) Cheng, F.; Fang, G. J.; Fan, X.; Huang, H. H.; Zheng, Q.; Qin, P. L.; Lei, H. W.; Li, Y. F. Enhancing the performance of P3HT:ICBA based polymer solar cells using LiF as electron collecting buffer layer and UV-ozone treated MoO3 as hole collecting buffer layer. *Sol. Energy Mater. Sol. Cells* **2013**, *110*, 63−68.

DOI: 10.1021/acsanm.9b00902
ACS Appl. Nano Mater. 2019, 2, 4942−4953